Azimuthal anisotropy of Hudson Bay using seismic interferometry

Agnieszka Pawlak and David W. Eaton

ABSTRACT

The Hudson Bay basin is the least studied of the four major Phanerozoic intracratonic basins in North America, which include the hydrocarbon-rich Williston, Illinois and Michigan basins. Using azimuthal anisotropy results in conjunction with isotropic group velocity maps from previous work, we can further focus our study on determining the formation and regional crustal structure beneath Hudson Bay. Twenty-one months of continuous ambient-noise recordings have been acquired from 37 broadband seismograph stations that encircle Hudson Bay. These stations are part of the Hudson Bay Lithospheric Experiment (HuBLE), an international project that is currently operating more than 40 broadband seismograph stations around the periphery of Hudson Bay. The inter-station group-velocity dispersion curves found from noise-generated seismic-interferometry studies, also know as ambient-noise tomography, are input into a tomographic inversion procedure producing images of crustal azimuthal anisotropy.

This study marks the first where ambient seismic-noise data have been considered in azimuthal anisotropy work. Our resolution testing suggests that the interpretation of the results requires some caution, but good path coverage is available. Preliminary results show a dominant southwest-northeast anisotropic direction, with weak correlation with the tectonic belts. In contrast, previous anisotropic studies have found that crustal anisotropy is strongly correlated with regional geology. Our results suggest that contributions from other forces may be important. Stresses, including large-scale regional stresses from plate motion are considered, but also show little correlation with our data. Local glacial isostatic rebound may be a contributing factor, but further work is required.

INTRODUCTION

Hudson Bay is a vast inland sea that overlies the Paleozoic Hudson Bay basin, an intracratonic basin with similar stratigraphic record to the hydrocarbon rich Williston, Illinois and Michigan basins. The processes of formation of the intracratonic basins such as Hudson Bay are poorly understood; this study seeks clues to achieve a better understanding of these processes by investigating regional crustal structure. Although the method of investigation, known as ambient noise tomography (or seismic interferometry) has been widely used in the past 5 years (e.g., Shapiro et al. 2005; Curtis et al., 2006; Yao et al., 2006; Yang et al. 2007; Moschetti et al. 2007; Lin et al. 2007, 2010), this study is one of the first to incorporate seismic anisotropy into the analysis.

In this paper we apply seismic interferometry to 37 broadband seismograph stations located around the perimeter of Hudson Bay (FIG 1) with continuous recording for 21 months. The present study builds on earlier work (Pawlak et al. 2010) in which we imaged the tectonic structure of the crust and upper mantle beneath Hudson Bay based on isotropic analysis (following Benson et al. 2007). Here, we describe the ambient-noise method briefly, followed by the anisotropy inversion method in more detail. Preliminary results and resolution reconstruction results are shown, followed by our interpretation and of the data. The basin-scale approach described here is also applicable to smaller-scale investigations

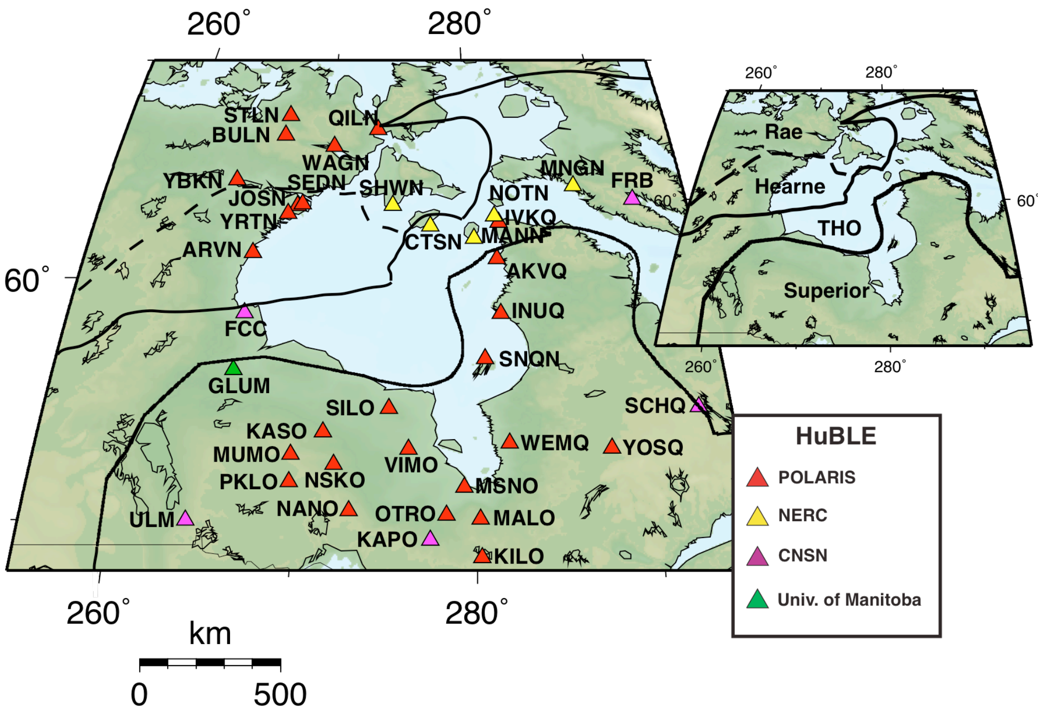

FIG 1. Map of Hudson Bay showing all HuBLE stations using in this study. Black lines represent approximate location of tectonic boundaries (after Eaton and Darbyshire 2010).

DATA AND PROCESSING METHODS

Continuous data from 37 broadband seismic stations installed around Hudson Bay have been analyzed. All stations are part of the HuBLE experiment aimed at understanding the subsurface beneath the Bay. Data were collected for 21 months, starting from September 2006 and ending May 2008. Raw data consists of three-component measurements of ground motion with a sampling rate of 40Hz.

Data processing procedures follows Bensen et al. (2007). First, data are cut into individual one-day records and resampled to 1Hz. Daily trends, means and instrument response are removed. Earthquake signals and instrument irregularities are also removed using a one-bit time normalization followed by spectral whitening and bandpass filtering between 0.005Hz and 0.3Hz. Once daily time series are processed, cross-correlations of the vertical component are preformed between all possible stations pairs and all available daily records. At this point, there remain 591 usable station pairs from a possible 666 pairs, based on data quality (FIG 2).

Usually, an average of the causal and acausal cross-correlation time lags are used for dispersion analysis. With significant asymmetry in each half (shown in FIG 2), we have adopted an approach in which either the causal or (time-reversed) acausal half is selected based on which has the higher signal-to-noise ratio (SNR). This SNR-based selection method yields better-defined dispersion ridges. The resulting one-sided correlation is called an empirical Green's function (EGF). Time-frequency analysis is used to estimate group-velocity dispersion curves for each EGF (FIG 3). Detailed processing procedure is described in Pawlak et al. 2010.

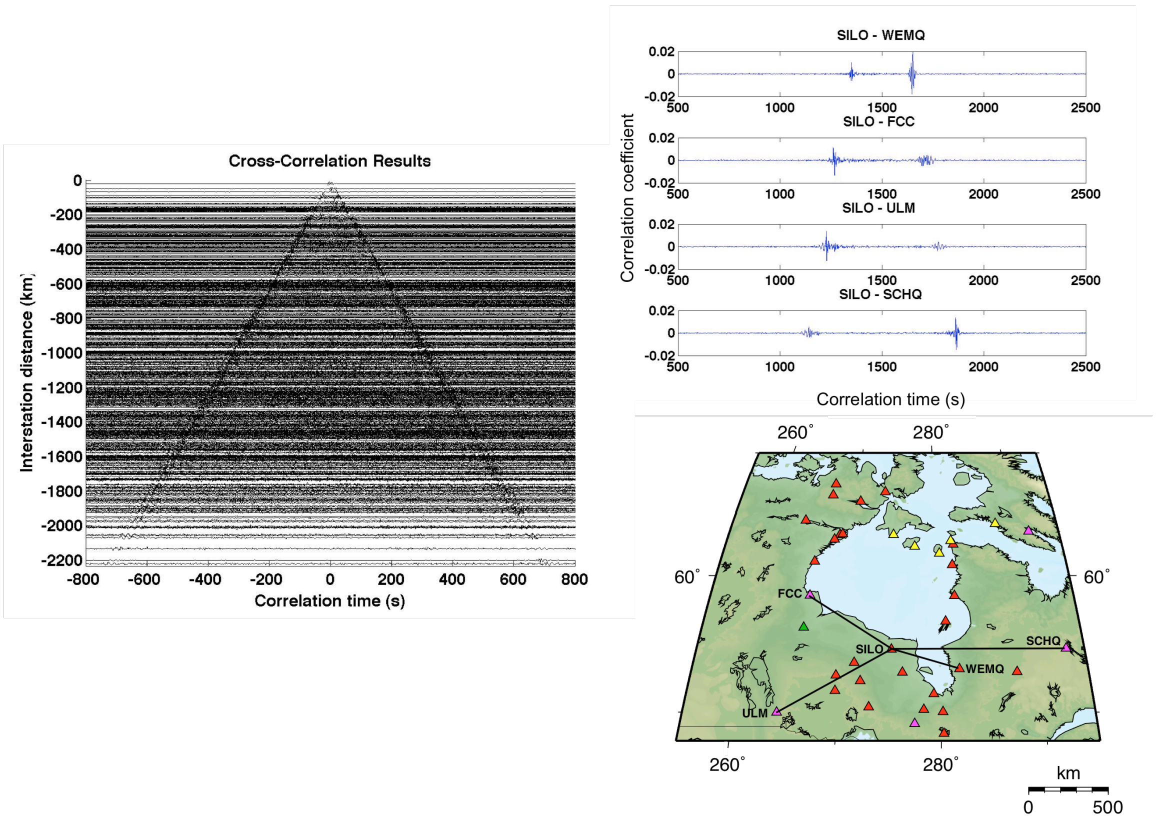

FIG 2. Stacked cross-correlations versus interstation distance for 591 two-station paths (left). Both positive and negative lags are shown. Examples of five cross-correlations (upper right) illustrates asymmetry of correlograms with respect to signal-to-noise ratio (SNR), typical of this dataset. Corresponding paths are shown in the lower right.

INVERSION

Tomographic inversion procedures used here follow the approach described by Darbyshire and Lebedev (2009). Working in a polar co-ordinate system defined by θ, ϕ, the tomographic inversion problem is described by:

$$\int_\theta \int_\phi K_i(\omega,\theta,\phi)\delta U(\omega,\theta,\phi)d\phi d\theta = \delta U_i(\omega) \pm \Delta U_i(\omega) \tag{1}$$

where $\delta U(\omega,\theta,\phi)$ is the group-velocity perturbation at (θ,ϕ) and frequency ω, $\delta U_i(\omega)$ and $\Delta U_i(\omega)$ are the measured inter-station average group-velocity anomaly and measurement error, respectively (note that phase velocity measurements contain an inherent $2\pi N$ ambiguity, where N is an integer). K_i defines the sensitivity kernel for the ith station pair; the reader is referred to Darbyshire and Lebedev (2009) for details.

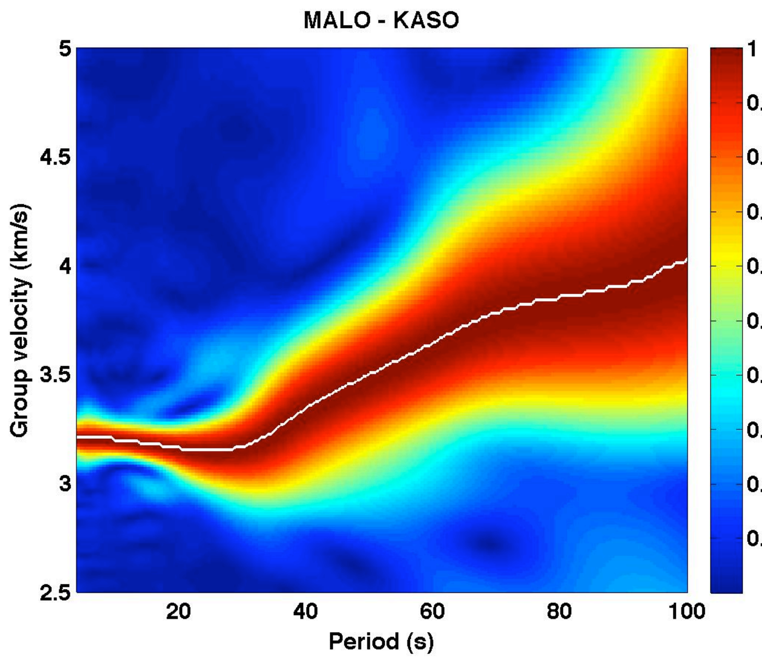

FIG 3. Example time-frequency plot and dispersion analysis. The colour scale shows the amplitude envelope, normalised for each period value. The while line represents the group-velocity dispersion curve used as input for the inversion procedure.

Differential sensitivity areas are complex, even if they are estimated with a first-order approximation in a laterally homogeneous Earth (Chervot and Zhao 2007), and thus will not be explored in depth at this point. We define $K_i(\theta,\phi)$ following Darbyshire and Lebedev (2009); at all frequencies $K_i(\theta,\phi)$ is defined the same, as zero-width rays along inter-station great-circle paths. In test inversions, finite-width rays are used. In this case, the cross-section perpendicular to the path of $K(\theta,\phi)$ are trapezoidal, with a constant kernel value in the center of the kernel and a gradual decrease to zero around the edges.

Solutions for each desired period are solved separately by using equation 1 for all usable measurements of $\delta U_i(\omega)$. This results in a system of linear equations that is solved using a LSQR algorithm (Paige and Saunders 1982) with smoothing and damping. Following Darbyshire and Lebedev (2010) and Lebedev and van der Hilst (2008), the region of interest is divided into an array of integration grid knots, with a dense inter-knot spacing of 40 km. A hexagon around each knot is defined, containing all (six) closest neighboring knots. The weight of the sensitivity kernel at each knot in the integral over the sensitivity area is found by calculating the sensitivity kernel, $K_i(\theta,\phi)$, at each knot and multiplying in by the hexagonal area. Smoothing and damping parameters for each knot point are also constrained by the anomaly variation between neighboring knots in the hexagonal area.

For weakly anisotropic media, the Rayleigh (or Love) velocity can be expressed as the sum of an isotropic component (δU_{iso}) and terms that describe the azimuthal variation (Smith and Dahlen, 1973):

$$\delta U(\omega) = \delta U_{iso}(\omega) + A_1(\omega)\cos(\Psi) + A_2 \sin(2\Psi) + A_3(\omega)\cos(4\Psi) + A_4(\omega)\sin(4\Psi) \tag{2}$$

where the '2Ψ' and '4Ψ' terms account for the π- and $\pi/2$-periodic variations, respectively, of velocity with wave-propagation azimuth Ψ. The 4Ψ signal is thought to be the dominant anisotropic term in the upper mantle where the symmetry is orthorhombic, whereas the 2Ψ is thought to be characteristic for crustal anisotropy. For this study we are focusing on crustal anisotropy, so the 4Ψ result is used solely for testing robustness of the isotropic and 2Ψ results with respect to the amount of 4Ψ signal allowed in the models.

RESULTS

Preliminary results are shown in FIG 4, for 20s and 30s periods. Red color represents lower isotropic velocities and blue represents higher isotropic velocities. The 20s period is mainly sensitive to a mid-crustal depths (~ 10-25 km), while 30s is sensitive to the lower crust (20-35 km). We see a low velocity region within the centre of Hudson Bay, as compared with the higher velocities that form a horseshoe shaped region that coincides with the Archean Superior craton (FIG 1). These isotropic results are consistent with tomographic results found in Pawlak et al. 2010, which are based on a different tomographic reconstruction method.

Black bars in FIG 4 show the 2Ψ anisotropy directions. We see significant difference in anisotropic direction between the 20s and 30s periods. The 20s period maps exhibit a predominately southwest-northeast direction, while the 30s period map is dominated by almost north-south fabric. In contrast to a recent study by Lin et al. (2010), these results show weak correlation to the regional tectonics as inferred from potential-field data (Eaton and Darbyshire, 2010). Another potential factor that could affect crustal anisotropy is the stress direction; this scenario is considered below.

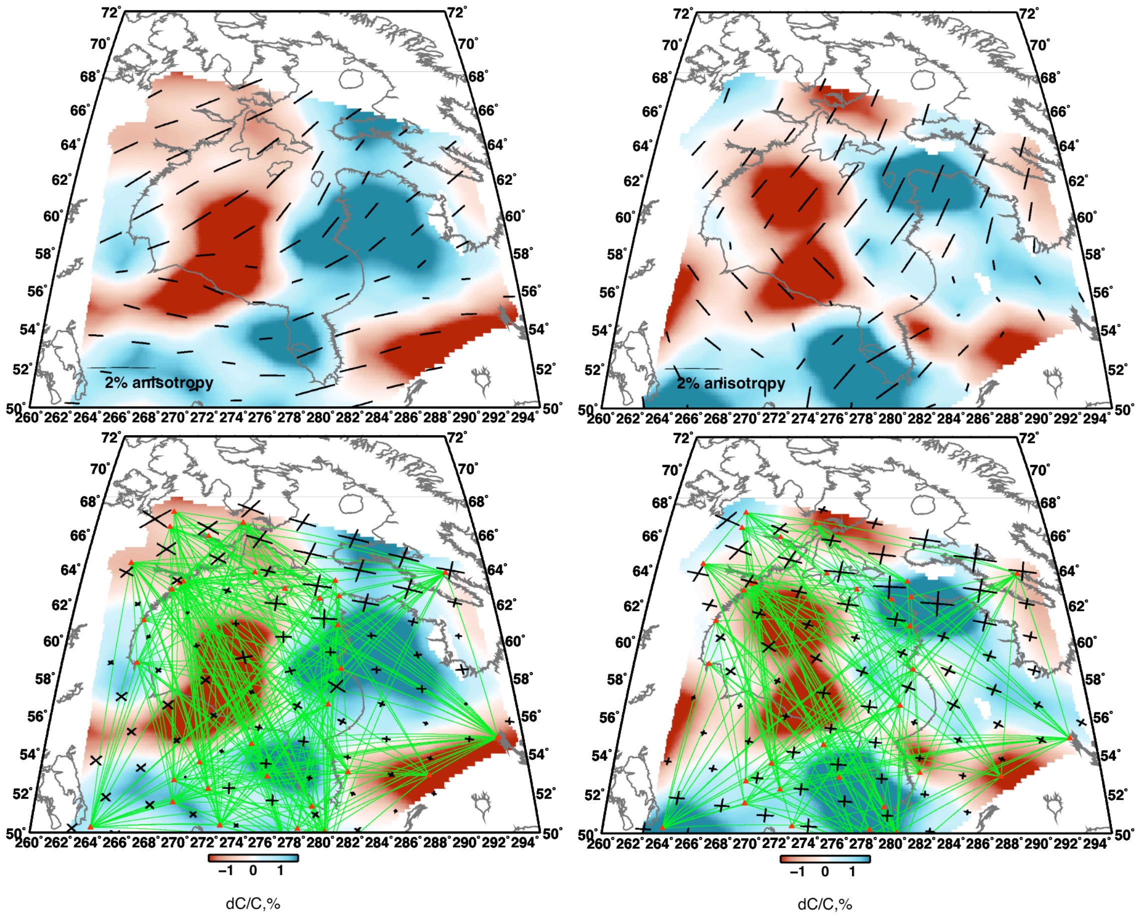

FIG 4. Tomographic maps for periods 20s and 30s. Isotropic velocities show in red (lower velocity) and blue (higher velocity). The upper panels correspond with 2Ψ anisotropy directions, shown with the black lines. The lower panels show 4Ψ anisotropy with black crosses and green lines show inter-station paths for the given period.

RESOLUTION TESTING

Before further interpretation of tomographic results, we first consider a series of resolution tests. We preformed two resolution tests, one to test the isotropic results and one to test the robustness of the anisotropic results. First, a purely isotropic "checkerboard" model was created, consisting of alternating high-velocity and low-velocity regions. By forward modeling, the checkerboard model was reconstructed using the same approach that was used to invert the observations. FIG 5 shows these results for 20s and 30s periods. An important element of this test is 'leakage' of the 2Ψ anisotropy into the model. As mentioned above, the model was purely isotropic, yet the results exhibit spurious anisotropy directions as well. The anisotropy is small, but it does show possible artifacts in the anisotropic results due to low path coverage. This can be seen on the upper right-hand side of both the 20s and 30s, where we have northwest-southeast trending anisotropy directions. This trend is small in amplitude, but must be taken into consideration when interpreting results.

The second resolution test preformed is for anisotropy. For this test the results from FIG 4 were used as the model, but the anisotropy directions were rotated by 90 degrees. Again, by forward modeling, we found the results in FIG 5 (lower panels). We find the inversion results to be robust, as if there was an artifact, we would see a rotation of about 90 degrees back to what we saw in the data results. Since the reconstruction is consistent with our model, we can say that the anisotropy results are most likely real.

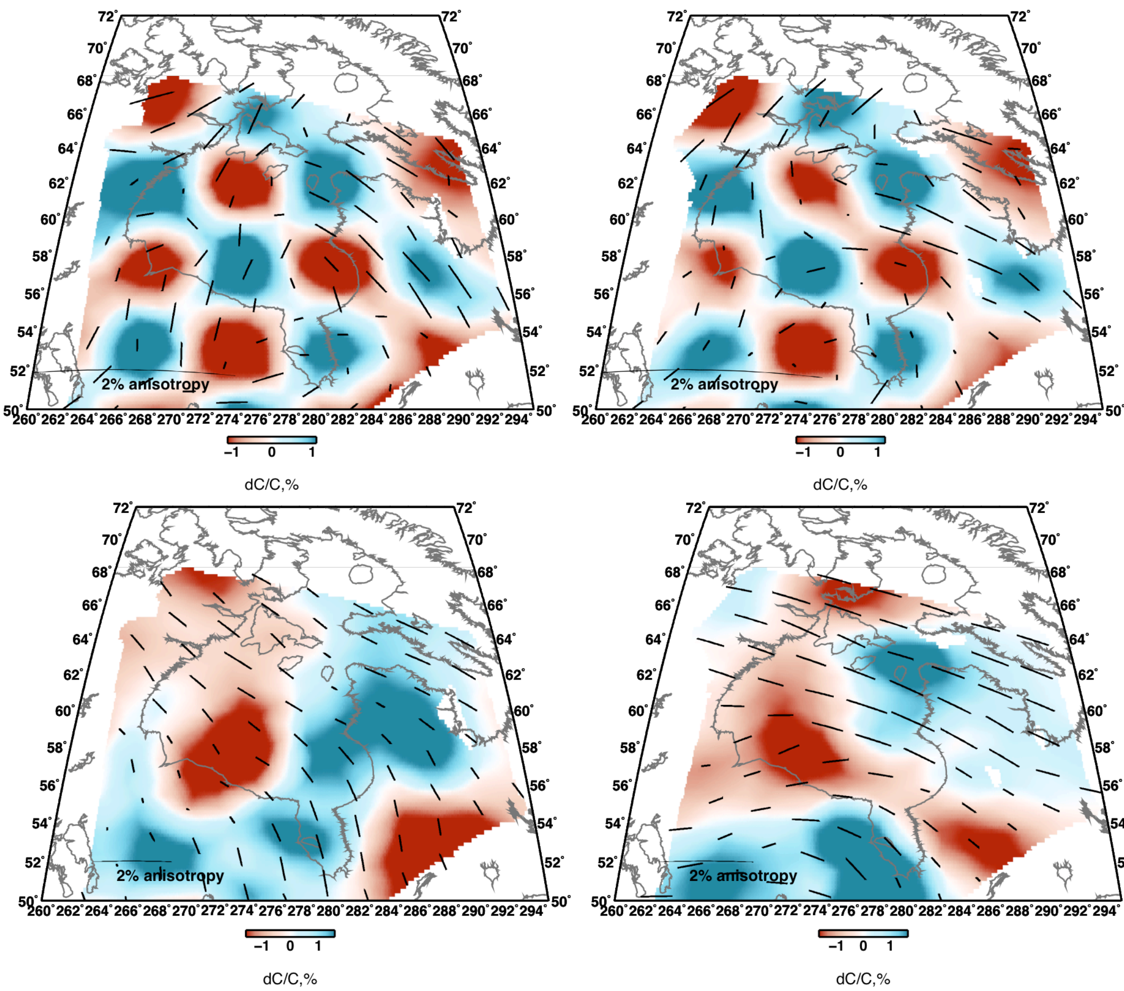

FIG 5. Checkerboard reconstruction results for periods 20s and 30s (upper panel). Anisotropy resolution reconstruction results for periods 10s, 20s and 30s. To test for artifacts in the anisotropy results, the reconstruction results from FIG 4 have been used, but the anisotropy results have been rotated by 90 degrees.

DISSCUSION

As noted above, seismic anisotropy in the crust could be affected by stress direction. As shown in Fig. 6, there is relatively sparse data, to constrain crustal stress directions in Hudson Bay (Heidback et al. 2008). As a proxy for crustal stress, we can turn to plate-motion direction, which is often parallel to the maximum stress direction. Using the plate motion using MORVEL2010 (DeMets et al. 2010) we see that the plate-motion direction across most of Hudson Bay is in an east-west direction (FIG 6). This also does not provide a very satisfactory fit to the observed data. This suggests that some other source of stress perturbation, perhaps related to glacial isostatic adjustment, may be a factor in this area.

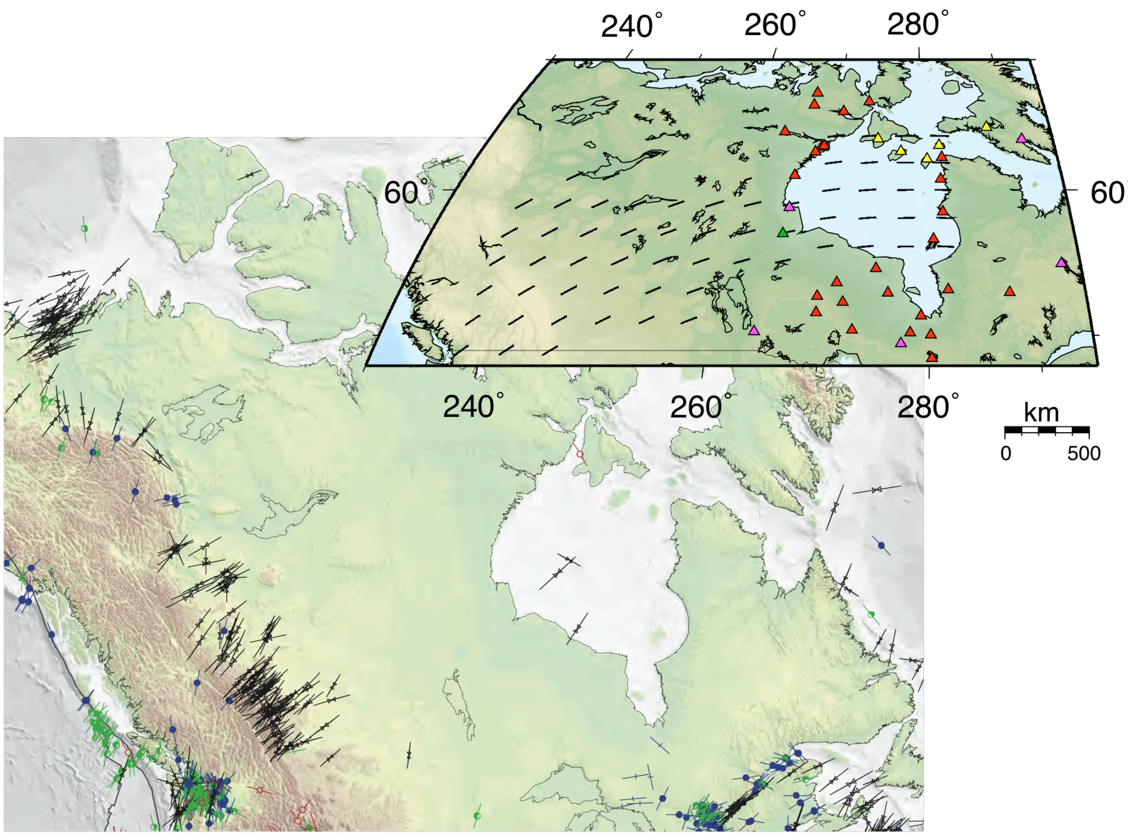

FIG 6. World Stress Map (modified from Heidback et al. 2008) and plate motion direction map of Canada (inset) calculated using MORVEL 2010 (DeMets et al. 2010).

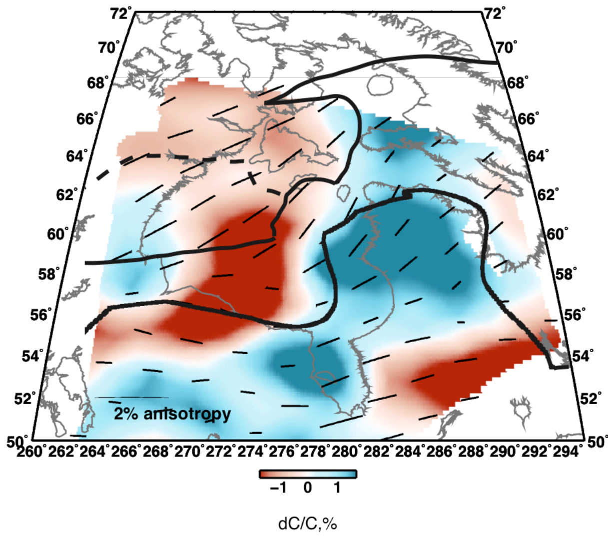

FIG 7. The 20s period map (from FIG 4) with tectonic boundaries superimposed.

ACKNOWLEDGEMENTS

We are grateful to Dr. Honn Kao, from the Pacific Geoscience Center in Sydney, B.C., for providing us with initial data and assistance with data processing. A special thank you to Sergei Lebedev for allowing us to use his inversion code and Fiona Darbyshire for all her help with everything from helpful input to debugging code. We thank other members of the HuBLE working group for stimulating discussions and the CREWES project and CREWES sponsors at the University of Calgary for their support. Thank you to C-NGO and the First Nation communities around Hudson Bay for allowing seismometer deployments. GMT (Wessel and Smith, 1995) and dispersion code written by R. Herrmann was used in the preparation of some figures. Natural Environment Research Council (NERC) stations, for this project, are supported by grant No. NE/F007337/1. This study was supported by NSERC through a Discovery Grant to DWE.

REFERENCES

Barmin, M.P., M.H. Ritzwoller, and A.L. Levshin, 2001, A fast and reliable method for surface wave tomography: Pure Appl. Geophys., 158, 1351 – 1375.

Bensen, G.D., Ritzwoller, M.H., Barmin, M.P., Levshin, A.L., Lin. F., Moschetti, M.P., Shapiro, N.M. and Yang, Y., 2007. Processing seismic ambient noise data to obtain reliable broad-band surface wave dispersion measurements: Geophys. J. Int, 169, 1351-1375.

Chervot, S. and L. Zhao, 2007, Multiscale finite-frequency Rayleigh-wave tomography of the Kaapvaal craton: Geophys. J. Int., 169, 201-215.

Curtis, A., P. Gerstoft, H. Sato, R. Snieder, and K. Wapenaar, 2006, Seismic interferometry – turning noise into signal: The Leading Edge, 1082-1092.

Darbyshire, F.A. and S. Lebedev, 2009. Rayleigh wave phase-velocity heterogeneity and multilayered azimuthal anisotropy of the Superior Craton, Onatrio; Geophys. J. Int., 176, 215-234.

DeMets, C., R.G. Gordon, and D.F. Argus, 2010, Geologically recent plate motions, *Geophys. J. Int.*, *181*, 1-80, doi:10.1111/j.1365-246X.2010.04491.x.

Eaton, D.W. and F.A. Darbyshire, 2010, Lithospheric architecture and tectonic evolution of the Hudson Bay region: Tectonophysics, 480, 1-22.

Heidback, O., M. Tingay, A. Barth, J. Reinecker, D. KerfeB and B. Muller, 2008, The World Stress Map database release 2008. Doi: 10.1594/GFZWSM.Rel2008.

Lebedev, S. and R.D. van der Hilst, 2008, Global upper-mantle tomography with the automated multimode inversion of surface and S wave forms: Geophys. J. Int., 173, 505-518.

Lin, F.C., M.H. Ritzwoller, J. Townend , M. Savage, and S. Bannister, 2007, Ambient noise Rayleigh wave tomography of New Zealand: Geophys. J. Int., 18.

Lin, F.C., M.H. Ritzwoller, Y. Yang, M.P. Moschetti and M.J. Fouch, 2010, The Stratification of seismic azimuthal anisotropy in the western US: Submitted to Nature Geoscience.

Moschetti, M.P., M.H. Ritzwoller, and N.M. Shapiro, 2007, Surface wave tomography of the western United States from ambient seismic noise: Rayleigh wave group velocity maps: Geochem., Geophys., Geosys., 8.

Paige, C.C. and M.A. Saunders, 1982, LSQR: an algorithm for sparse linear equations and sparse least squares: Assoc. Comput. Mach. Trans. Math. Software, 8, 43-71.

Pawlak, A.P., D.W. Eaton, I.D. Bastow, J.M. Kendall, G. Helffrich, J. Wookey and D. Snyder, 2010, Crustal structure beneath Hudson Bay from ambient-noise tomography: Implications for basin formation: Submitted to Geophys. J. Int.

Shapiro, N.M., M. Campillo, L. Stehly, and M.H. Ritzwoller, 2005, High resolution surface wave tomography from ambient seismic noise: Science, 307, 1615-1618.

Smith, M.L. and F.A. Dahlen, 1973, The azimuthal dependence of Love and Rayleigh wave propagation in a slightly anisotropic medium: J. geophys, Res., 78, 3321-3333.

Yang, Y., M.H. Ritzwoller, A.L. Levshin, and N.M. Shapiro, 2007, Ambient noise Rayleigh wave tomography across Europe: Geophys. J. Int., 168, 259

Yao, H., R.D. van der Hilst, and M.V. de Hoop, 2006, Surface-wave tomography in SE Tibet from ambient seismic noise and two-station analysis: I.- Phase velocity maps: Geophys. J. Int., 166, 732-744.